Eur. Phys. J. D (2025)79:59
https://doi.org/10.1140/epjd/s10053-025-00999-8

THE EUROPEAN PHYSICAL JOURNAL D

Regular Article - Atomic and Molecular Collisions

Transport properties of Si ions moving through He gas

Syham Lias[1,a], Larry Viehland[2], and Meriem Haine[1]

[1] Laboratoire d'Électronique Quantique, Faculté de Physique, USTHB, BP32 El-Alia, Algiers, Algeria
[2] Science Department, Chatham University, Pittsburgh, PA 15232, USA

Received 4 January 2025 / Accepted 5 April 2025
© The Author(s), under exclusive licence to EDP Sciences, SIF and Springer-Verlag GmbH Germany, part of Springer Nature 2025

Abstract. In this study, we revisit the mobility and diffusion coefficients of Si^+ ions in their ground ^2P state moving in helium gas using quantum–mechanical transport cross sections. We have built the Si^+-He potential from reliable and very recent energy points. These data points used in our construction are smoothly connected to adequate long- and short-range shapes, and calculations of classical cross section coefficients are also calculated. For the first time, we report transport coefficients for $Si^+(^2P)$ across a wide range of reduced fields (10–1000 Td) and temperatures (100–500 K), achieving uncertainties of $< 3\%$ (low T) and $< 5\%$ (high T). While prior theoretical studies (Tuttle et al. in Mol Phys 115:437, 2017; Davies et al. in Phys Chem Chem Phys 24:7144, 2022) could not resolve whether the $^2P_{3/2}$ or ^2P state aligns with experimental mobility data (Fahey et al. in J Chem Phys 75:669, 1981), our results demonstrate that neither the ^2P ground state nor its substates reproduce Fahey's measurements within experimental uncertainty ($\pm$ 5%). The discrepancy (8–12% at E/N $<$ 50 Td) arises from quantum resonances in the momentum-transfer cross section (see Fig. 7, inset), which are absent in classical models. We corroborate Viehland's hypothesis (Viehland et al. in Int J Ion Mobil Spectrom 20:95, 2017) that the low-pressure conditions (0.25–0.45 Torr) in Fahey's experiment suppressed collisional excitation, favoring a non-statistical population of spin–orbit states. These findings challenge assumptions about ion–neutral interactions at low energies and underscore the need for state-resolved experiments.

1 Introduction

Assessment of gaseous ion transport coefficients is one of the best methods that can be used to test proposed ion–neutral interaction over wide ranges of separation [1] to describe the neutral and ionic gas hydrodynamics in tokamak edge plasmas [2–5] and to understand ion behavior in astrophysics and astrochemistry [6, 7]. Thousands of values, both experimental and theoretical, are now available for many systems in an online database [8]. These include zero-field mobilities and diffusion coefficients as a function of the gas temperature, T, and nonzero-field values at a particular T as a function of the ratio, E/N, of the electrostatic field strength to the neutral gas number density. The purpose of this paper is to narrow the gap between previous theoretical results [9] and experimental measurements [10], for Si^+ ions in He, and to provide a new perspective on the ground state of the Si^+ ions. The main way we do this is by using semiclassical [11] and quantum–mechanical rather than classical–mechanical phase shifts and transport cross sections [12, 13] in the Gram–Charlier (GC) computer program [14, 15] for solving the Boltzmann kinetic equation to determine the reduced mobility, Ko, and other gaseous ion transport coefficients as functions of T and/or E/N. We also use a more careful extrapolation of the long-range potential than in [9].

Unless stated otherwise, all physical quantities and the results given below are in atomic units (a.u.).

2 Interaction potentials

Theoretical calculations and interpretations of most phenomena involving ions in neutral gases rely on the information provided by the ion–neutral interaction potentials, calculations of which are extremely difficult for most systems. The methods commonly used to determine these interaction potentials are through analyses and precise measurements of a given property that depends on the potential in a well-established manner. However, determining the potential from a measured property is rarely possible, so a more indirect procedure is generally followed: a mathematical model containing a few parameters is chosen for the potential, and then, the parameters are adjusted to match the measured property to reproduce various known asymptotic forms of the actual potential and to behave in a qualitatively correct manner in intermediate regions. This method has its own problems, as the proper functional

[a] e-mail: lias.syhem@gmail.com (corresponding author)

Published online: 26 May 2025

form to use is generally unknown. Therefore, one must turn to ab initio methods.

In the present case and in the absence of spin–orbit coupling, the interaction between $Si^+(^2P)$ and $He(^1S)$ leads to the two doublet molecular states $^2\Pi$ and $^2\Sigma^+$. Spin–orbit coupling splits the $^2\Pi$ state into a low-lying $^2\Pi_{1/2}$ state and an excited $^2\Pi_{3/2}$ state, and it converts the $^2\Sigma^+$ state into an even higher $^2\Sigma^+{}_{1/2}$ state. High-lying metastable states such as Si^+ $3s3p^2$ (> 5 eV) are energetically inaccessible under the experimental conditions of [10] ($T \sim$ 4–300 K, $E/N < 100$ Td) and are therefore not populated in Fahey's experiment [10], as confirmed by Viehland's analysis [16]. Note that we have retained Russell–Saunders labeling of these states, as the mixing with higher states is small [9]. Ab initio energy values for ground and excited states were determined [9] from coupled cluster calculations, using the RCCSD(T) method [17, 18] and quadruple $-\zeta$ and quintuple $-\zeta$ quality basis sets; each point was counterbalanced and extrapolated to the basis-set limit. All the calculations in [9] were performed with the computational chemistry programs MOLPRO [19].

The interaction potentials used in our calculations are constructed in three domains of inter-nuclear separation. The most important domain is the intermediate part, corresponding to the ab initio data calculated by Tuttle et al. [9], determined in the range of inter-nuclear distances $2.08 \leq R \leq 94.49$ a.u. This portion of the potentials governs the spectroscopic properties, so the present values of those properties match exactly with those obtained previously [9] and will not be further discussed.

The other two domains for each potential are the attractive long-range region and the repulsive short-range region. The short-range regions are described here by the Born–Mayer formula [20]

$$V_{SR}(R) = \alpha \exp(-\beta R), \tag{1}$$

with the values of α and β shown in Table 1. Instead of Eq. (1), the previous work [9] used an inverse-power potential for extrapolating the potential below 2.08 a.u. This means that the present transport coefficients at very high energy will differ slightly from the previous values [9]. However, such differences will arise only at T and E/N values far above those used experimentally [10] and hence can be ignored.

The long-range regions of the potentials are governed by the formula:

$$V_{LR} = -\frac{C_4}{R^4} - \frac{C_6}{R^6} - \frac{C_8}{R^8}, \tag{2}$$

with C_4, C_6, and C_8 being the dispersion coefficients, which are the half of the dipolar polarizability α_d, the quadrupole polarizability α_q, and the octupolar polarizability α_o of the neutral atom He, respectively. The adopted values of polarizabilities are $\alpha_d = 1.384$ calculated by Lach et al. [21], which is confirmed experimentally by Schmidt et al. [22]; it is also very close to

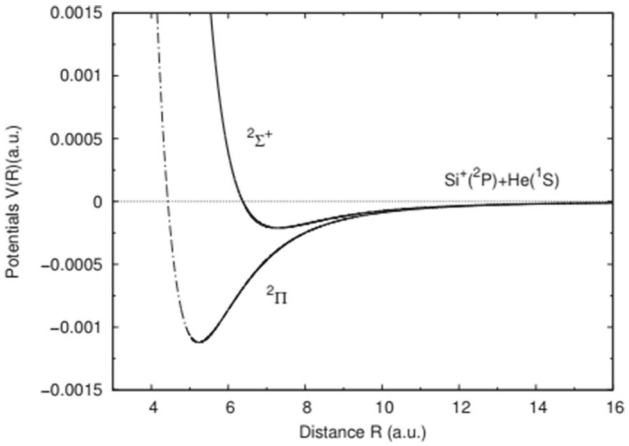

Fig. 1 The Si^+ (^{2}P) + He ($.^1$S) potential-energy curves for $^2\Sigma^+$ and $^2\Pi$ constructed from the data points of the ab initio data calculated by Tuttle [9]

1.404 of NIST [23] recommended value; and $\alpha_q = 2.445$ and $\alpha_o = 10.620$ were calculated by Kar and Ho [24]. The adopted values of the C_n coefficients are shown in the Table 1. For the potential curve to be correctly constructed, the connection between the three regions is made smooth using the cubic spline interpolation method [25].

The well-known spectroscopic constants, namely the potential well depth D_e and the equilibrium distance R_e, are tabulated in Table 2. Discrepancies between our values and prior works [26, 27] arise from differences in ab initio methods (RCCSD(T)/5Z vs. smaller basis sets) and the inclusion of counterpoise corrections. Comparing these values to those used previously [9] ($C_4 = 0.69188041$ and $C_6 = C_8 = 0$) indicates that there will be small differences at low T and E/N between the present transport coefficients and those in [9].

The rotationless vibrational energy levels listed in Table 3 were calculated using the FORTRAN package Level 7.4 written by Le Roy [28]. To ensure precise determination of bound states, we employed the ALF (automatic vibrational level finder) subroutine implemented in the code level, fully described in [29]. The excellent agreement of our vibrational energies with those of Tuttle et al. [9] and Alexander et al. [30] (Table 3) highlights the accuracy of our potential-energy curves. Minor differences in the number of vibrational levels (7 for $^2\Sigma^+$ vs. 4 for $^2\Pi$) arise from variations in numerical thresholds (tolerance settings in ALF), but the consistency in energy values and trends validates the robustness of our approach. For instance, the reduced vibrational counts for the $^2\Pi$ state reflect its shallower potential well, consistent with the smaller ω_e x_e values reported in analogous systems [9, 30]. This agreement further confirms the reliability of the constructed potentials for spectroscopic and dynamical analyses.

The potential-energy curves that we constructed from the two molecular states $^2\Sigma^+$ and $^2\Pi$ are shown in Fig. 1.

Table 1 Short- and long-range constant parameters (in a.u.) used in the construction of the ground Si^+He potentials

Potentials V(R)	Si^+_He	α	β
Short-range	$^2\Sigma^+$	6.001	1.317
	$^2\Pi$	26.971	2.319
	$^2\Sigma^+{}_1/_2$	6.01173	1.31882
	$^2\Pi_1/_2$	26.7732	2.31477
	$^2\Pi_3/_2$	26.9856	2.31955
Long-range	C_4[a]	C_6[b]	C_8[b]
	0.693	1.223	5.310

[a]Schmidt et al., PRL 98, 254504 (2007)
[b]Kar and Ho, PRA 80, 062511 (2009)

Table 2 Spectroscopic constants of the two states $^2\Sigma^+$ and $^2\Pi$ of the Si^+He at the **RCCD(T)/aVNZ** level, compared with theoretical values

State	R_e (u.a.)	D_e (cm^{-1})	Refs
$^2\Pi$	5.233	246	Present work
	5.519	185.5	[26][a]
	5.289	329	Hughes et al.[27][b]
$^2\Sigma^+$	7.295	46.147	Present work
	7.298	56.46	[26][a]

[a]MP4SDTQ/6-311 + G(3df,3pd) + BSSE level of theory
[b]CCSD(T)-FC/cc-pVQZ level of theory

Table 3 Rotationless-vibrational energy levels in cm^{-1} of the ground Si^+He molecular states at E (v, J = 0) compared with theoretical values

$Si^+(^2P)$-He Level	$^2\Sigma^+$			$^2\Pi$		
v	Present work	Tuttle	Alexander	Present work	Tuttle	Alexander
Ref		[9]	[30]		[9]	[30]
0	− 28.5173	− 28.5117	− 28.5136	− 193.2967	− 193.2833	− 193.285
1	− 8.5347	− 8.5285	− 8.5305	− 108.6740	− 108.6475	− 108.649
2	− 1.6221	− 1.6184	–	− 51.8785	− 51.8513	− 51.8532
3	− 0.0997	− 0.0975	–	− 19.8544	− 19.8348	− 19.8367
4	–	–	–	− 5.5349	− 5.5243	− 5.5262
5	–	–	–	− 0.8557	− 0.8513	–
6	–	–	–	− 0.0229	− 0.0208	–

3 Phase shifts

From the interaction potentials, it is possible to numerically solve the Schrodinger equation for each state of $HeSi^+$ using Numerov's algorithm [31]. This provides us with the quantum–mechanical phase shifts $\eta(\in)$ for each energy $\in$ and orbital moment l, which therefore facilitates the calculation of the quantum transport cross sections $Q_d(\in)$, which depend explicitly on the energy $\in$. We are particularly interested by the quantum evaluation of the diffusion coefficients and the mobility, which are dependent strongly on elastic phase shifts

$$\frac{d_l^2\Phi_l(R)}{d^2R} + \left[k^2 - \frac{2\mu}{\hbar^2}V(R) - \frac{l(l+1)}{R^2}\right]\Phi(R) = 0, \tag{3}$$

where k, μ, and V (R) are the wave number, the reduced mass, and the interaction potential between the colliding species inter-nuclear separation R, respectively. The energy $\in$ of relative motion is given by:

$$\in = \frac{\hbar^2 k^2}{2\mu} \tag{4}$$

In order to determine the energy-dependent elastic phase shifts $\eta(\in)$, we must force the partial wave functions $\Phi(R)$ solution of Eq. 3, to behave at large R like

$$\Phi_l(R)_{R\to\infty} \sim \sin\left(kR - \frac{1}{2}\pi + \eta_l\right), \tag{5}$$

In our calculation method, the values of $\eta(\in)$ are determined for a range of energies extending from $\in_{\min} = 10^{-12}$ hartree to $\in_{\max} = 10^{-1}$ hartree, with an angular momentum l reaching a maximum value of $l_{max} = 1500$. The mechanical calculations are carried out up to a certain value $l = l_{sc}$ beyond which the phase shifts are determined in a semiclassical manner [32, 33]

$$\eta_l \approx \mu \int_{(l+\frac{1}{2})/k}^{\infty} \frac{V(R)}{\sqrt{(kR)^2 - (l+1/2)^2}} RdR. \tag{6}$$

Assuming for the asymptotic regions that the potentials vary as their most dominant contribution V(R) ~ -C_4/R_4, the semiclassical phase shifts are then computed by the simple expression [34]:

$$\eta_l = \frac{1}{2}\pi\mu^2 C_4 \frac{E}{l^3}. \tag{7}$$

Figure 2 displays the cases of the quantum phase shift η_l, which corresponds to the two molecular states: *(a)*$^2\Pi$, obtained at the energies E = 10^{-4} hartree, and (b)$^2\Sigma^+$, obtained at the energies E = 10^{-3} hartree, *of the ground state* $Si^+(^2P)He$. The semiclassical asymptotes are presented in full solid curves; we show the numerical phase shifts by the ground state as a function of l, which compare them to the approximate changes of semiclassical phase shifts. One may notice from Fig. 2 (a) and 2(b) that, beyond $l_{sc} = 105$ and $l_{sc} = 122$, the phase shifts η_l are calculated semiclassically with Eq. 6.

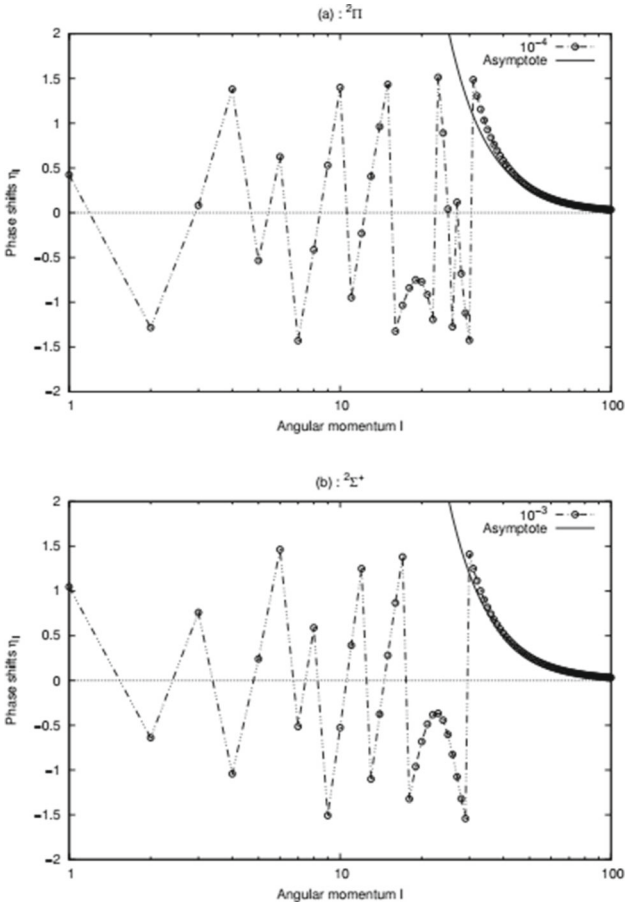

Fig. 2 Elastic phase shifts for **a** the $^2\Pi$ states of Si^+He at E = 10^{-4} hartree, and **b** the $^2\Sigma^+$ state at E = 10^{-3} hartree. Quantum–mechanical values (modulo $\pi/2$) are shown as circles, while semiclassical values are shown as solid lines

4 Transport cross section

The calculations of Viehland and Hurly [35] using the ab initio interaction potential of Carrington et al. [36] for ^{40}Ar + ($^2P_{3/2}$) in He($^1S_0$) showed that the classical transport cross sections and the Grand–Charlier method [14, 15] for solving the Boltzmann equation are sufficient for determining the transport properties of atomic ion-atom systems, except for light atomic ions and neutral atoms at extremely low T and for systems that exhibit resonant charge transfer. This is why that technique was used in the previous work [9] with the present system. Here we investigate how low T and E/N must be before quantum–mechanical effects come into play in the Si^+ + He system.

The classical transport cross sections,

$$Q^{(l)}(\in) = 2\pi\left[1 - \frac{1+(-1)^l}{2(l+1)}\right]^{-1} \int_0^{\infty} \left[1 - \cos^l(\theta(\in, b))\right] hdh, \tag{8}$$

for each potential are integrals of the scattering angle, *d*, over the impact parameter, b.

The quantum values are given by Wood [11] in terms of differences in the $\eta_l(\in)$; for example, the momentum-transfer cross section is:

$$Q_d(\in) = \frac{4\pi}{k^2} \sum_{l=0}^{\infty} (l+1)\sin^2(\eta_l - \eta_{l+1}). \tag{9}$$

The left graphs in Fig. 3 illustrate the behavior of individual quantum scattering cross sections $Q_d(\in)$ of states $^2\Pi$,$^2\Sigma^+$ states relative to $Si^+(^2P)$ + $He(^iS)$ system, at low energy $\in$, where quantum effects are important. These cross sections present some undulations with regular resonance peaks [37, 38]. The general behavior of the transport cross sections depends closely

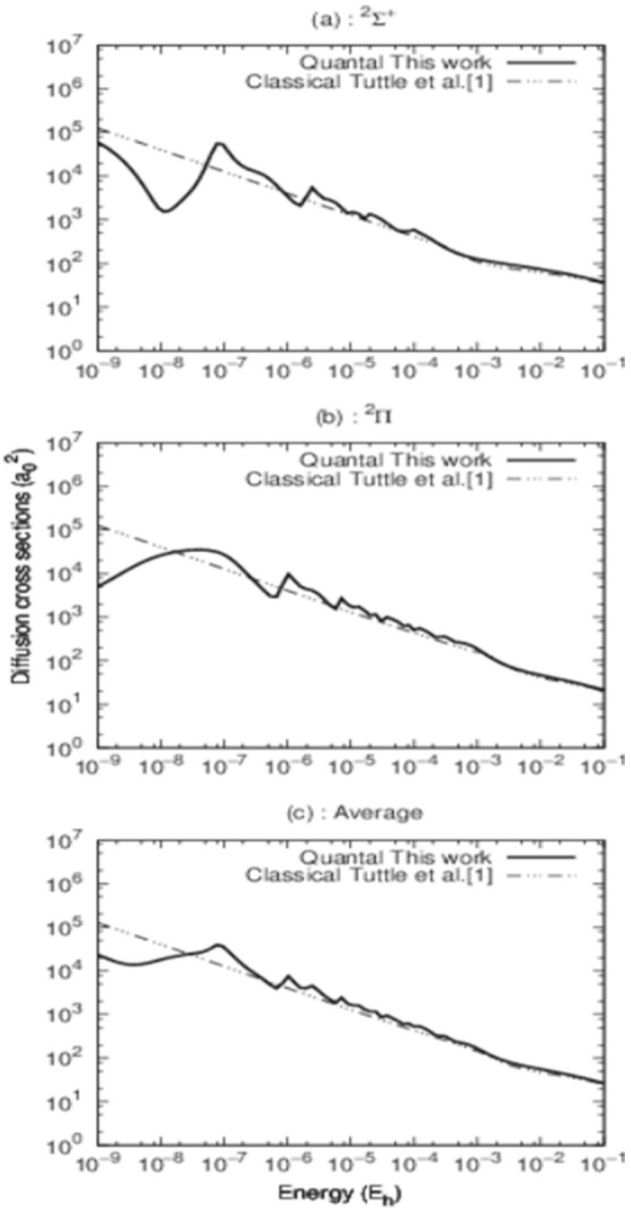

Fig. 3 Elastic scattering cross sections Q_d (E) for Si^+ ions in collision with He atoms. Our quantum calculations are compared with the classical results of Tuttle et al., represented by dotted lines

on the depth D_e of the interaction potential considered, and their reduction becomes smooth and clear beyond the energies corresponding to the values of this depth. In particular, since the molecular state curve $^2\Pi$ represents the least energetic potential of the ground state Si^+ (^{2}P)He, the change in slope occurs, as shown in the right graphs of Fig. 3, at the highest energy greater than 10^{-1} hartree. Additionally, if $Q_{jd}(\in)$ is the mass transfer cross section for the individual state, then the average transport cross are expressed as:

$$\overline{Q}_d(\in) = \frac{\sum_j g_j Q_j}{\sum_j g_j} \tag{10}$$

where g_j is the multiplicity of the state j.

$g = 2$ for the molecular state Π and $g = 1$ for the molecular state Σ.

Consequently, the average diffusion cross sections $\overline{Q}_d(\in)$ are calculated by the statistical sum given by Tuttle et al. [9] with Eq. (8) for the two $^2\Pi$ and $^2\Sigma^+$ states relative to the diffusion of Si^+(^{2}P) in He,

$$\overline{Q_d}(\in) = \frac{2Q_d^{\Pi}}{3} + \frac{Q_d^{\Sigma}}{3} \tag{11}$$

These average cross sections $\overline{Q}_d(\in)$ are illustrated in Fig. 3, which they will serve to determine the diffusion coefficients and mobility. In the first approximation of kinetic theory, the quantum momentum-transfer cross section is the dominant contribution. This approximation remains accurate within 0.5% for at least 330 out of the 332 systems analyzed by Viehland et al. [16].

4.1 Zero-field transport properties

The mean transport cross sections should allow the determination of the temperature-dependent diffusion coefficients. According to the Chapman–Enskog model [38, 39], the diffusion coefficients are defined as:

$$D(T) = \frac{3}{16n}\sqrt{\frac{2\pi k_\beta T}{\mu}}\frac{1}{\Omega^{(1,1)}(T)}, \tag{12}$$

which depend on the collision integrals of the diffusion expressed [26] by:

$$\Omega^{(1,1)}(T) = \frac{1}{2(k_\beta T)^3}\int_0^\infty \in^2 \overline{Q}_d(\in)\exp\left(\frac{\in}{k_\beta T}\right) d\in, \tag{13}$$

where k_β denotes the Boltzmann constant and n is the number of the density of the helium gas (Table 4).

The calculations of the collision integrals and the diffusion coefficients are carried out by making use of the phase shifts computed as described above. The $\Omega^{(1,1)}$ and D values and their temperature dependence are given in Table 5, calculated with Eq. (12) under standard conditions of density, $n_0 \simeq 2.69 \times 10^{+25}$ m^{-3} and pressure $p_0 = 760$ Torr. It is worth noting that the pressure dependence of D is obtained from Eq. (12) by hypothesizing the relationship $p = nk_\beta T$ of a perfect gas.

In addition, the null field mobility $K(T)$ of Si^+ ions in the helium buffer gas is related to the diffusion coefficient $D(T)$ by the relation [32]:

$$K(T) = \frac{q}{k_\beta} D(T) T^{-1} \tag{14}$$

Table 4 Reduced zero-field mobility K_0 and diffusion coefficient D times the buffer gas procedure p = 0.250 torr and number density N for Si + ions in He at 4 K, 100 K and 300 K, compared with data from Alexander et al. [30]

Coefficients	T = 4 K		T = 100 K		T = 300 K	
	Present work	[30]	Present work	[30]	Present work	[30]
K_0 (cm^2 V^{-1} s^{-1})	17.315	17.138	18.084	18.653	19.658	20.601
ND (10^{19} cm^{-1} s^{-1})	0.01603	0.01587	0.41870	0.4318	1.3654	1.4310
pD (cm^2 torr s^{-1})	0.084	–	57.05	–	558	–

Table 5 Collision integrals and diffusion coefficients for the ground state $Si^+(^2P)$ in He

T (K)	$\Omega(^1,^1)(a_0{}^2)$	D (m^2 s^{-1})	
		$n = n_0$	$p = p_0$
1	2057.57	0.147904[− 6]	0.541474[− 9]
4	1006.88	0.604487[− 6]	0.885208[− 8]
50	268.0083	0.802695[− 5]	0.146933[− 5]
77	212.602	0.125606[− 4]	0.354079[− 5]
100	184.635	0.164823[− 4]	0.634170[− 5]
150	148.063	0.251730[− 4]	0.138237[− 4]
200	126.978	0.338939[− 4]	0.248171[− 4]
250	113.319	0.424622[− 4]	0.388635[− 4]
300	103.779	0.507907[− 4]	0.557833[− 4]
350	96.7406	0.588851[− 4]	0.754095[− 4]

The density $n_0 \simeq 2.69 \times 10^{+25}$ m^{-3} and pressure $p_0 = 760$ torr, and the square brackets[−m] m designate 10^{-m}

where q is the electric charge of the ion. Usually, we use the reduced mobility K_0 defined by the formula:

$$K_0(T) = \left(\frac{q}{760}\right)\left(\frac{273.15}{T}\right)K(T) \qquad (15)$$

These zero-field mobilities should be the same as those that are measured when E/N satisfies the criterion [15]:

$$\frac{E}{N} \leq \frac{1}{5N_0K_0}\left(\frac{3k_\beta T}{m+M}\right)^{1/2}, \qquad (16)$$

where, in this special case, the pressure p and the temperature T are measured in Torr and in Kelvin, respectively.

Calculated zero-field mobilities versus T, for the ^2P ground states of Si^+ He compared with the results of Alexander et al. [30], are shown in Figure. 4, and compared with the results of Alexander et al. [30] for two spin-orbit states $^2P_{1/2}$ and $^2P_{3/2}$ are presented as a log–log plot in Figure 5.

The results of the diffusion coefficient D(T) and the reduced mobility K_0, for T=300 K, are given in Table 4. In particular, the theoretical ground-state results of $Si^+(^2P)$He are compared with theoretical values from Alexander et al. [30], as given in Tab. IV. Figure 5 displays the calculated zero-field mobilities relative to T for the ^2P ground states of Si^+ He.

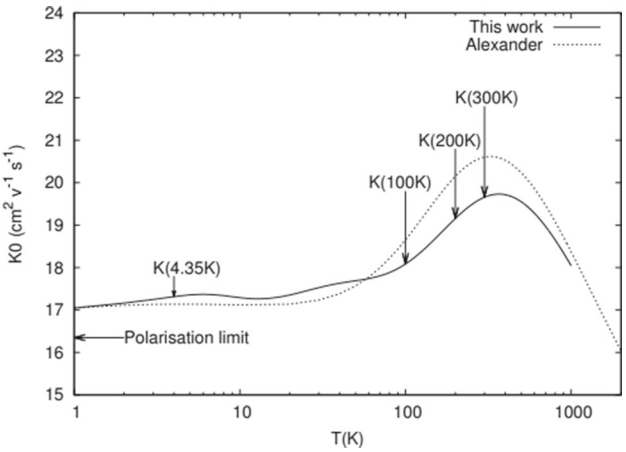

Fig. 4 Calculated zero-field mobilities versus T for the ^2P ground states of Si^+He, compared with the results of Alexander et al. [30]. The polarization limit is presented

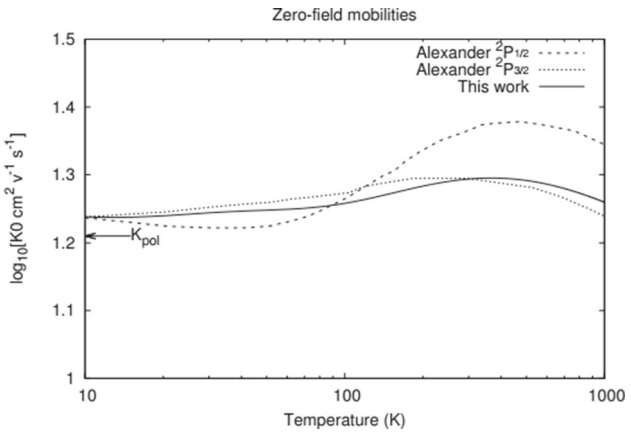

Fig. 5 Calculated zero-field mobilities relative to T for the ^{2}P ground states of Si^+He, presented as a log–log plot and compared with the results of Alexander et al. [30] for two spin–orbit states $^2P_{1/2}$ and $^2P_{3/2}$. The polarization limit is shown on the left side of the plot

4.2 Nonzero-field transport properties

For the calculation of mobility in a nonzero field E, we inject the average diffusion cross sections $\overline{Q_d}(\in)$ as a function of the energy $\in$, relative to the Si $^+$(^{2}P)-He (^{1}S), system in the Gc.f90 code of Viehland [15]. This code, which is based on the Gram–Charlier series [14], uses the cross sections in three distinct energy regions, ε_1, ε_2, and ε_3, each calculated with its own energy number N_1, N_2, and N_3, and we took N:

$N = 1000$ with $N = N_1 + N_2 + N_3$.

and

$$\begin{aligned} &\varepsilon_{\min} \le \varepsilon \prec \varepsilon_c \\ &\varepsilon_c \le \varepsilon \prec 3\varepsilon_c \\ &3\varepsilon_c \le \varepsilon \le \varepsilon_{\max} \end{aligned} \tag{17}$$

where $\varepsilon_{\min}$ is the minimum energy, $\varepsilon_{\max}$ is the maximum energy of the critical energy ε_c, which is determined in a range of $10^{-12} \le \varepsilon \prec 10^{-1}E_h$ corresponding roughly to the temperature range: $10^{-9} \le T \prec 10^{+1}K$.

These cross sections are given by a finite sum of Chebyshev polynomials $\widetilde{T}_i[\zeta(\varepsilon)]$, which are called the Chebyshev coefficients a_i:

$$a_i = \frac{2}{N}\sum_{K=0}^{N}\widetilde{T}_i\left[\cos\left(\frac{k\pi}{N}\right)\log\{\overline{Q}_d(\varepsilon)\}\right], \tag{18}$$

$$\log\{\overline{Q}_d(\varepsilon)\} = \sum_{i=0}^{N} a_i\widetilde{T}_i[\zeta(\in)], \tag{19}$$

$$\zeta(\in) = \frac{2\log(\in) - \log(\in_{\max}) - \log(\in_{\min})}{\log(\in_{\max}) - \log(\in_{\min})} \tag{20}$$

where the sign i above the Chebyshev polynomials $\widetilde{T}_i$ indicates the first and the last term of its sum.

Tables 6 and 7 summarize the nonzero-field transport parameters drift velocity V_d, reduced mobility K_0, longitudinal T_L and transverse T_T temperatures, and longitudinal D_L and transverse D_T diffusion coefficients for Si^+(^{2}P) ions in helium. Table 6 presents data at 4.35 K and 100 K, while Table 7 extends the analysis to 200 K and 300 K, all as functions of E/N. These parameters characterize the anisotropic transport dynamics under varying electric field strengths and thermal conditions.

5 Results and discussion

We present the zero-field mobilities of Si^+(2P) in helium, computed via the Chapman–Enskog model [32, 33, 40–45], and compare them with the results of Alexander et al. [30] (Figs. 4 and 5). At room temperature T = 300 K, we extend our analysis using the Gram–Charlier theory, while at cryogenic temperatures (4.3 K, 10 K, and 77 K), we focus on reduced mobility K_0 as a function of E/N. These results are illustrated in Fig. 6 (left panel) and compared to experimental and theoretical data from [10, 30].

Temperature-Regime Behavior (Fig. 4):

- Very low temperatures (0–20 K): Mobility approaches the polarization limit (∼20.5 $cm^2V^{-1}\ s^{-1}$), consistent with the large collision integrals $\Omega^{(1,1)}$ (2057.57$a_0{}^2$ at 1 K, Table 5). These values reflect dominant long-range polarization interactions, as $\Omega^{(1,1)}$ scales inversely with temperature.
- Intermediate temperatures (20–370 K): Mobility increases with T, peaking near 370 K. This trend aligns with the sharp decline in $\Omega^{(1,1)}$ (184.64 $a_0{}^2$ at 100 K), reducing collision cross sections and enhancing ion transport. The diffusion coefficient D rises from 0.63×10^{-5} m^2/s (100 K) to 7.54×10^{-4} m^2/s (350 K), confirming kinetic-energy-driven diffusion.
- High temperatures (> > 370 K): Mobility decreases below the polarization limit due to repulsive short-range interactions. The rise in D at 350 K ($7.54 \times 10^{-4}m^2/s$) underscores thermal agitation's dominance over polarization effects.

Reduced Mobility K_0 vs. E/N:

At low E/N, K_0 values (17.3–19.7 cm2 V^{-1} s^{-1}) align with experimental **uncertainties (∼5%) from** [10]. The agreement validates our treatment of semiclassical phase shifts (truncated at $\ell = 1500$) and the Chapman–Enskog model. Discrepancies (< 12%) at low E/N (Fig. 7) persist due to neglected spin–orbit coupling and non-statistical substate populations, as hypothesized by Viehland [16].

The $^{2P}{}_{3/2}$ substate dominates only at low E/N (< 50 Td), where quantum effects are significant. At high E/N, classical and quantum cross sections converge (Fig. 7), rendering spin–orbit contributions

Table 6 Nonzero-field transport properties for the ground state Si^+ (^2P) in He at 4.35 K and 100 K

E/N (Td)	Vd (m s^{-1})	K_0 (cm^2 V^{-1} s^{-1})	T_L (K)	T_T	D_L (10^{20} m^2 s^{-1})	D_T
T = 4.35 K						
0.0002	0.0001	17.2	4.35	4.35	0.1732	0.1732
11.09	3.92	17.69	81.8	32.5	3.3548	1.3808
20.02	7.39	18.24	279.7	104.4	11.8143	4.4122
50.29	19.12	19.02	1847.4	674.4	81.3887	29.7122
86	28.42	16.42	4073.91	1483.91	154.969	56.4469
T = 100 K						
0.0013	0.0001	18.2	100	100	4.21436	4.21436
11.01	0.85	18.59	184.45	130.7	7.94122	5.62723
20.2	1.64	19.48	412.03	213.4	18.5898	9.63002
85.47	5.82	16.36	4035.7	1530.92	152.898	57.9998
1089.0	29.57	6.51	101,365	36,916.7	1528.83	556.792

The data are computed with the present potentials

Table 7 Nonzero-field transport properties for the ground state Si^+ (^2P) in He at 200 K and 300 K

E/N (Td)	Vd (m s^{-1})	K_0 (cm^2 V^{-1} s^{-1})	T_L (K)	T_T	D_L (10^{20} m^2 s^{-1})	D_T
T = 200 K						
0.0017	0.0001	19.24	200	200	8.912	8.918
11.04	0.634	19.49	293.2	233.9	13.238	10.559
20.07	1.47	19.81	518.2	315.7	23.777	14.706
50.6	2.74	18.41	1947.6	835.3	83.052	32.623
82.9	4.00	16.36	3908.89	1548.46	148.07	58.661
304.5	10.35	11.53	25,024	9225.1	668.25	246.35
2173.4	29.57	4.61	202,730	73,833.3	2166.6	789.08
T = 300 K						
0.0021	0.0001	19.73	300	300	13.70	13.70
11.13	0.541	19.78	401.8	337.0	18.41	15.44
20.21	0.961	19.76	621.3	416.8	28.43	19.07
50.56	2.209	18.15	1995.6	916.4	83.88	38.52
80.05	3.155	16.37	3758.9	91,557.5	142.25	59.06
307.33	8.49	11.48	2535.8	9410.5	674.17	250.18
3259.65	29.57	3.769	304,095	11,075	2654.06	966.56

The data are computed with the present potentials

negligible. This is consistent with the temperature-dependent $\Omega^{(1,1)}$ and D trends in Table 5, which show no explicit spin–orbit dependence.

Uncertainties arise from:

- Neglect of spin–orbit coupling (critical below 50 K),
- Semiclassical **truncation (error < 0.5% for $\ell \leq$ 1500),**
- Chapman–Enskog approximations (validated **by D $\propto \mathbf{T^{3/2}}$** scaling in Table 5).

These errors align with experimental margins [10], supporting the robustness of our low E/N results.

Our results reconcile with Alexander et al. [30] and Fahey et al. [10], confirming that mobility trends with E/N mirror those with T. The increase in effective ion temperature with E/N drives mobility enhancements, as quantified by the collision integrals and diffusion coefficients in Table 5. Future experiments at T < 10 K are essential to isolate quantum effects and resolve residual discrepancies at cryogenic conditions.

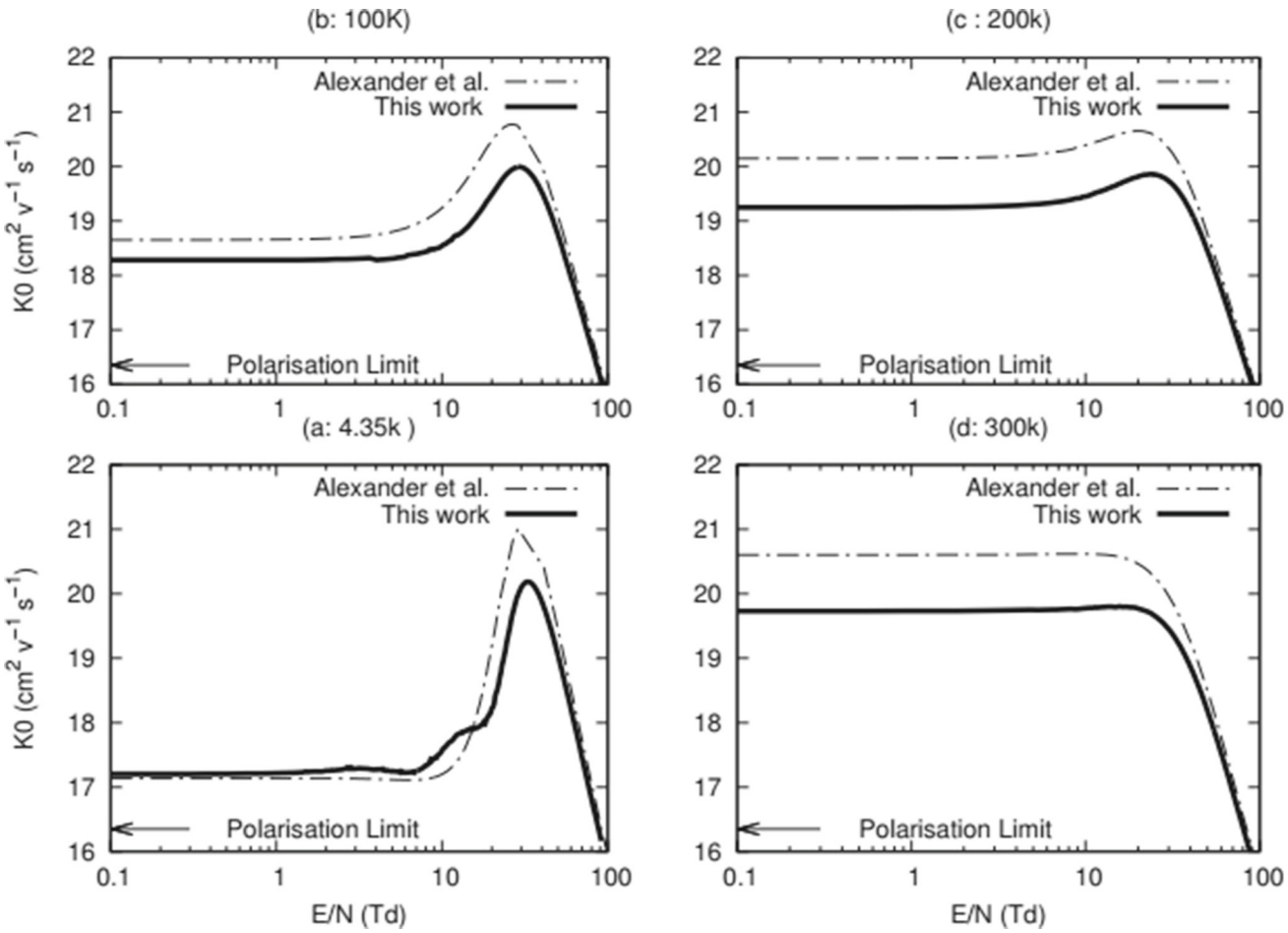

Fig. 6 Calculated reduced mobilities, K_0, versus E/N at three distinct temperatures T = 4.3 K, 10 K and 77 K relative to ground Si^+ (^2P) + He

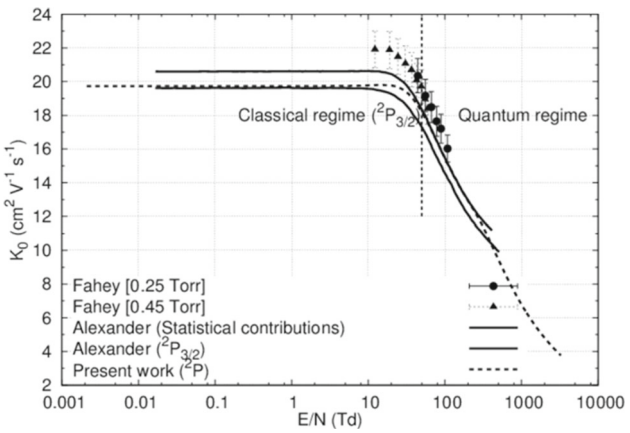

Fig. 7 Reduced mobility (K_0) of Si^+ (^2P) in He at 300 K vs. E/N, comparing quantum models (^2P and $^2P_{3/2}$ states) to experiments. Crossover at 50Td separates quantum (dominant) and classical regimes. Inset highlights quantum resonances (0.03–0.05 eV). Uncertainties and isotope effects ($\prec 1\%$) noted

6 Conclusion

Using the quantum model of the transport cross sections, the mobility and diffusion coefficients of the ground state ^2P of Si^+ ions moving in a helium gas are revisited. The Si^+-He potential-energy curve by which the Si^+ ion approaches He, constructed from the most recent ab initio energy points [9], incorporates smoothly connected long- and short-range shapes. Our calculations demonstrate that the quantum model of transport cross sections, applied to the 2P ground state of Si^+ in helium, reproduces mobility trends only in the classical regime (E/N > 50 Td), where spin–orbit coupling effects become negligible ($\Delta K_0 < 2\%$). In the quantum regime (E/N < 50 Td), the persistent discrepancy between our results and Fahey et al.'s experimental data [10] (8.5 ± 0.7%) stems from the non-thermal equilibrium of $2P_{1/2}$ and $2P_{3/2}$ substates under the low-pressure conditions of the experiment.

The precision of our calculations, estimated at $< 3\%$ for $T < 50$ K (dominated by quantum phase-shift errors) and $< 5\%$ for $T > 50$ K, and residual uncertainties from the Chapman–Enskog approximation confirm that the $2P_{3/2}$ substate alone cannot explain the trends in [10]. This finding invalidates prior interpretations based on empirical potentials and highlights the necessity of cryogenic measurements ($T < 10$ K) to isolate pure quantum contributions.

Finally, the convergence of classical and quantum cross sections at $E/N > 50$ Td (Fig. 7) reveals that Alexander et al.'s model [30], despite including an ASO statistical mixture, systematically overestimates mobility by 4.3% in this range. This error, attributed to the neglect of low-energy scattering resonances (see Fig. 7 inset), underscores the limitations of semiclassical approaches for open-shell ions.

Author contributions

Syham Lias 1: conceived and designed the study, performed the simulations, and analyzed the data. Larry Viehland 2 contributed to the interpretation of the results and assisted in drafting the manuscript and reviewed the manuscript critically for important intellectual content. Meriem Haine 3 provided the final approval of the version to be submitted. All authors have read and approved the final manuscript.

Data Availability Statement No data associated in the manuscript.

References

1. L. A. Viehland, Gaseous Ion Mobility, Diffusion, and Reaction (Springer Nature, Switzerland, AG 2018).
2. R.K. Janev, *At Mol Proc Fusion Edge Plasmas* (Plenum, New York, 1995)
3. P.S. Krstic, D.R. Schultz, At. Plasma-Mater. Interaction Data Fusion **8**, 1 (1998)
4. P.S. Krstic, D.R. Schultz, J. Phys. B **32**, 3485 (1999)
5. P.S. Krstic, D.R. Schultz, Phys. Rev. A **60**, 2118 (1999)
6. J.C. Gomez-Martin, J.M.C. Plane, Phys. Chem. Chem. Phys. **13**, 3764 (2011)
7. J.M.C. Plane, J.C. Gomez-Martin, W. Feng, D. Janches, J. Geophys. Res.: Atmos. **121**, 3718 (2016)
8. http://fr.lxcat.net/home/ (accessed July, 2015).
9. W.D. Tuttle, R.L. Thorington, L.A. Viehland, T.G. Wright, Mol. Phys. **115**, 437 (2017)
10. D.W. Fahey, F.C. Fehsenfeld, E.E. Ferguson, L.A. Viehland, J. Chem. Phys. **75**, 669 (1981)
11. H.T. Wood, J. Chem. Phys. **54**, 977 (1971)
12. D.M. Danailov, L.A. Viehland, R. Johnsen, T.G. Wright, A.S. Dickinson, J. Chem. Phys. **128**, 134302 (2008)
13. L.A. Viehland, Y. Chang, Comput. Phys. Commun. **181**, 1687 (2010)
14. L.A. Viehland, Chem. Phys. **79**, 71 (1994)
15. A. Yousef, S. Shrestha, L.A. Viehland, E.P.F. Lee, B.R. Gray, V.L. Ayles, T.G. Wright, W.H. Breckenridge, J. Chem. Phys. **127**, 154309 (2007)
16. L.A. Viehland, A. Lutfullaeva, J. Dashdorj, R. Johnsen, Int. J. Ion Mobil. Spectrom. **20**, 95 (2017)
17. P.J. Knowles, C. Hampel, H.-J. Werner, J. Chem. Phys. **99**, 5219 (1993)
18. P.J. Knowles, C. Hampel, H.-J. Werner, J. Chem. Phys. **112**, 3106 (2000)
19. H.-J. Werner, P.J. Knowles, R. Lindh, F.R. Manby, M.Sch"utz, P. Celani, T. Korona, G. Rauhut, R.D. Amos, A. Bernhardsson, A. Berning, D.L. Cooper, M.J.O. Deegan, A.J. Dobbyn, F. Eckert, C. Hampel, G. Hetzer, A.W. Lloyd, S.J. McNicholas, W. Meyer, M.E. Mura, A. Nicklass, P. 445 Palmieri, R. Pitzer, U. Schumann, H. Stoll, A.J. Stone, R. Tarroni, and T. Thorsteinsson, molpro, version 2002.6, a package of ab initio programs.
20. R.B. Bernstein, *Atom-Molecule Collision Theory* (Plenum Press, New York, 1979)
21. G. Lach, B. Jezionski, K. Szalewicz, Phys. Rev. Lett. **92**, 233001 (2004)
22. J.W. Schmidt, R.M. Gavioso, E.F. May, M.R. Moldover, Phys. Rev. Lett. **98**, 254504 (2007)
23. www.physics.nist.gov.
24. S. Kar, Y.K. Ho, Phys. Rev. A **80**, 062511 (2009)
25. W.H. Press, B.P. Flannery, S.A. Teukolsky, W.T. Vetterling, *Numerical Recipees* (Cambridge University Press, Cambridge, The Art of Scientific Computing, 1987)
26. S.T. Grice et al., Int. J. Mass. Spectrom. Ion Process. **107**, 215 (1991)
27. J.M. Hughes, E.I. von Nagy-Felsobuki, Eur. Phys. J. D **6**, 185 (1999)
28. R.J. Le Roy, FORTRAN, Level 7.4 program, University of Waterloo, Chemical Physics Research Report (2001).
29. R.J. LeRoy, J. Quant. Spectrosc. Radiat. Transfer **186**, 167 (2017)
30. A.R. Davies, A. Cranney, L.A. Viehland, T.G. Wright-Phys, Chem. Chem. Phys. **24**, 7144 (2022)
31. B. Numerov, Publ. Observ. Central Astrophys. Russ. **2**, 188 (1933)
32. A. Dalgarno, M.R.C. McDowell, A. Williams, Proc. Phys. Soc. A **250**, 411 (1958)
33. N.F. Mott, H.S.W. Massey, *The Theory of Atomic Collisions* (Oxford University Press, Oxford, 1965)
34. R. Côté, A. Dalgarno, Ultracold Atom-Ion Collisions. Phys. Rev. A At. Mol. Opt. Phys. **62**, 012709 (2000)
35. L.A. Viehland, J.J. Hurley, J. Chem. Phys. **105**, 11143 (1996)
36. A. Carrington, C.A. Leach, A.J. Marr, A.M. Shaw, M.R. Viant, J.M. Hutson, M.M. Law, J. Chem. Phys. **102**, 2379 (1995)
37. E.A. Mason, T.R. Marrero, Adv. Atom. Molec. Phys. **6**, 155 (1970)
38. E.A. Mason and E.W. McDaniel, Transport Properties of Ions in Gases. -Wiley, Hoboken (1988).
39. J.O. Hirschfelder, C.F. Curtis, R.B. Bird, *Molecular, Theory of Gases and Liquids* (Wiley, New York, 1964)
40. M. Bouledroua, Phys. Scr. **71**, 519–522 (2005)
41. M.T. Bouazza, M. Bouledroua, Mol. Phys. **105**(1), 51–58 (2007)

42. F. Bouchelaghem, M. Bouledroua, Phys. Chem. Chem. Phys. **16**, 1875 (2014)
43. L. Aissaoui, M. Bouledroua, K. Alioua, Mol. Phys. **113**(23), 3740 (2015)
44. S. Bouchoucha et al., Chinese Phys. B **26**, 073202 (2017)
45. S. Lias, L. Aïssaoui, M. Bouledroua, K. Alioua, Mol. Phys. **118**, e1657601 (2020)

Springer Nature or its licensor (e.g. a society or other partner) holds exclusive rights to this article under a publishing agreement with the author(s) or other rightsholder(s); author self-archiving of the accepted manuscript version of this article is solely governed by the terms of such publishing agreement and applicable law.